J. Fluid Mech. (1966), *vol.* 26, *part* 1, *pp.* 145–161
Printed in Great Britain

Hydrodynamic stability of the boundary layer on a continuous moving surface

By F. K. TSOU†, E. M. SPARROW
University of Minnesota, Minneapolis, Minnesota
AND E. F. KURTZ
Massachusetts Institute of Technology, Cambridge, Massachusetts

(Received 30 August 1965 and in revised form 12 January 1966)

The characteristics of the laminar boundary layer on a continuous moving surface are described and an experiment is performed to demonstrate that such a flow is physically realizable. The hydrodynamic stability of the flow is analysed within the framework of small-perturbation stability theory. A complete stability diagram is mapped out. The critical Reynolds number is found to be substantially higher than that for the Blasius flow and, correspondingly, the critical layer lies closer to the wall. The disturbance amplitude function and its derivative are numerically evaluated, from which are derived the vector flow field of the disturbance, the resultant flow field (main flow plus disturbances), the root-mean-square distributions of the disturbance velocity components, and the distributions of the kinetic energy and the Reynolds stress. The energy criterion for stability is also investigated and is found to be consistent with the solutions of the eigenvalue problem.

1. Introduction

In recent years, consideration has been given to a somewhat novel type of boundary-layer flow that is designated by Sakiadis (1961*a*, *b*, *c*) and by Koldenhof (1963) as the boundary layer on a continuous moving surface. A model of this flow situation is shown in the left-hand diagram of figure 1. As pictured in the figure, an unending plane sheet issues from a slot and moves to the right through an otherwise quiescent fluid environment. The velocity of the sheet is constant. Owing to the motion of the sheet, a fluid flow is induced. With increasing downstream distance from the slot, the region of induced flow penetrates deeper and deeper into the environment. In other words, the thickness of the boundary layer, shown as a dashed line in the figure, increases in the direction of motion of the surface.‡ As will be described later, the present authors have demonstrated by experiment that such a flow is physically realizable.

† Present address: Drexel Institute of Technology, Philadelphia, Pennsylvania.

‡ It has been pointed out to the authors that a similar situation occurs in the wall boundary layer behind a shock wave moving into a stationary fluid (e.g. as in a shock tube). If the co-ordinates are fixed with respect to the shock, then the wall moves and the boundary layer grows in the direction of motion, see Mirels (1961).

The aforementioned may be contrasted with the boundary-layer growth in the conventional Blasius flow. Consider a semi-infinite flat plate moving through an otherwise quiescent fluid. In this case, it is readily understood that the boundary layer grows in a direction that is opposite to that in which the plate is moving. Thus, the continuous-surface boundary layer displays a growth characteristic just reversed from that of the Blasius flow.

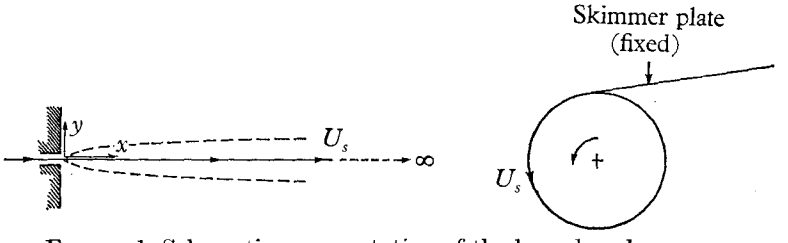

FIGURE 1. Schematic representation of the boundary layer on a continuous moving surface.

The laminar boundary layer on a continuous moving surface has been analysed by Sakiadis (1961*b*). It was shown that, by a similarity transformation, the momentum equation reduces identically to the Blasius equation. However, the boundary conditions differ from those of the Blasius problem, and, correspondingly, the solution is different.

The present investigation is concerned with the hydrodynamic stability of the boundary layer on a continuous moving surface. The analysis makes use of small-perturbation stability theory together with a numerical method for solving the resulting eigenvalue problem. A complete stability diagram is mapped out that shows not only the neutral stability curve but also includes amplification-factor contours. The critical Reynolds number marking the onset of instability is deduced from such a diagram. Disturbance amplitude functions are computed for stable, neutral, and unstable conditions. With these, the disturbance velocity components are evaluated. The vector velocity field of the disturbance is mapped out, and the resultant flow field (main flow plus disturbance) is constructed. In addition, the distributions of the root-mean-square velocity fluctuations, the kinetic energy, and the Reynolds stress are determined. Attention is then turned to the energy-balance equation, wherein the stabilizing dissipative term is opposed by the de-stabilizing Reynolds stress term. The aforementioned balance is evaluated both on and adjacent to the neutral stability curve.

2. The mainflow velocity profile

The starting point for the analysis of the laminar velocity field is the boundary-layer momentum equation and the continuity equation. The co-ordinates x and y are illustrated in the left-hand diagram of figure 1, and the corresponding velocity components are U and V. By employing a similarity transformation as follows

$$\eta = y\sqrt{\{U_s/(\nu x)\}}, \quad \psi = \sqrt{(\nu x U_s)}\,F(\eta), \tag{1}$$

the aforementioned conservation laws reduce to the Blasius equation, that is

$$F''' + \tfrac{1}{2}FF'' = 0. \tag{2}$$

Furthermore, by differentiation of the stream function ψ, one obtains

$$U = U_s F', \quad V = \tfrac{1}{2}\sqrt{(\nu U_s/x)}\,(\eta F' - F). \tag{3}$$

At the moving surface ($y = 0$), the no-slip condition of viscous flow requires that $U = U_s$. Moreover, the streamwise component of the velocity vanishes in the ambient fluid, that is, as $y \to \infty$. The foregoing, taken together with the impermeability condition $V = 0$ at $y = 0$, lead to

$$F(0) = 0, \quad F'(0) = 1, \quad F'(\infty) = 0. \tag{4}$$

The boundary conditions on $F'(0)$ and $F'(\infty)$ are just reversed relative to those of the classical Blasius problem.

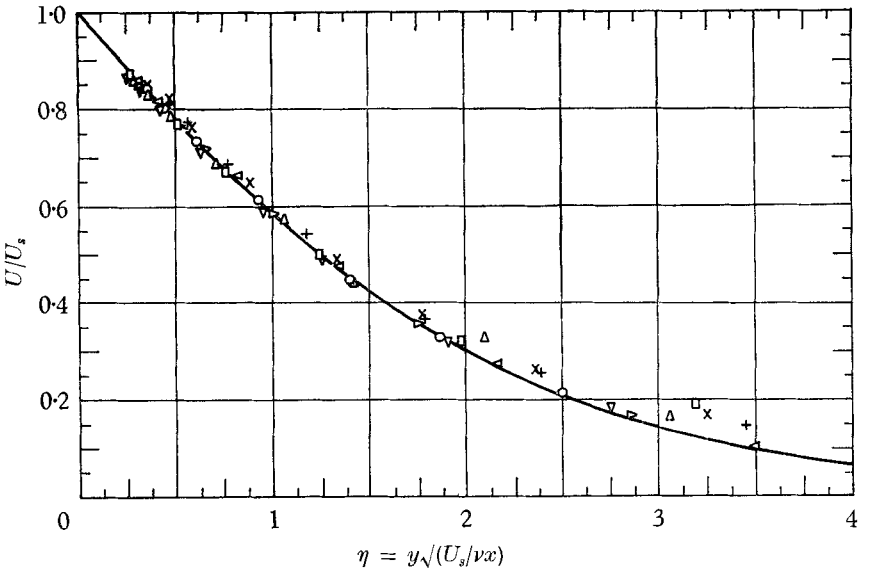

FIGURE 2. Boundary-layer velocity profile.

	x (in.)	U_s (ft./sec)		x (in.)	U_s (ft./sec)
○	2·67	34·3	◁	4·76	44·7
△	4·86	34·3	□	5·86	44·7
▽	5·96	34·3	+	2·57	53·6
▷	2·57	44·7	×	4·76	53·8

The solution of equation (2) subject to the boundary conditions (4) is readily accomplished by computer methods and need not be dwelled upon here. The value of $F''(0)$ needed for the numerical forward integration is found to be $-0{\cdot}44375$. Other characteristics of the velocity solution that are useful in the forthcoming stability analysis are the displacement thickness δ^* and the boundary-layer thickness δ. The latter is defined as the distance from the wall at which U/U_s has diminished to approximately 0·1 per cent. These quantities are, respectively,

$$\delta^* = 1{\cdot}616\sqrt{(\nu x/U_s)}, \quad \delta = 9{\cdot}36\sqrt{(\nu x/U_s)}. \tag{5}$$

Another result that stems from the solutions is the fact that the transverse velocity V is negative; that is, there is an inflow from the environment into the boundary layer. In contrast to this, the transverse velocity in the conventional Blasius flow is positive.

As a prelude to the stability analysis, it may be of interest to describe briefly an experiment that was performed by the authors to verify the physical reality of the boundary-layer flow just analysed. The details of the experiment may be found in the dissertation of Tsou (1965) from which this paper is drawn. In essence the continuous moving surface was modelled by a 12 in. diameter rotating drum shown in the right-hand diagram of figure 1. A skimmer plate, fixed in space, was employed to create the boundary-layer flow. Velocity profiles were measured with a flattened impact probe that was arranged to move normal to the cylinder at various circumferential locations.

The velocity profiles thus determined are shown in figure 2 along with a solid line that represents the analytical solution. The abscissa is the similarity variable. The various symbols denote measurement stations situated at different distances from the skimmer plate and different surface speeds U_s. The x co-ordinate employed in the figure is corrected to account for any initial boundary-layer development on the skimmer. Inspection of the figure shows that not only are the data for the various conditions unified by the use of the similarity variable, but also that there is very good agreement between analysis and experiment. The data tend to fall slightly above the curve at the larger values of η; this is believed to be caused by disturbances in the room. In the opinion of the authors, the experiment just described demonstrates that the boundary layer on a continuous moving surface is a physically realizable flow.

3. The stability problem

The formulation of the stability problem follows along lines that are well documented for boundary-layer flows, for instance, Schlichting (1960). For purposes of analysis, the mainflow is regarded as a parallel flow. Upon this are superposed two-dimensional disturbances u', v' and p' that are functions of the co-ordinates x, y and the time t. It is assumed that both the mainflow and the resultant flow (mainflow plus disturbances) satisfy the Navier–Stokes equations. Moreover, those inertia terms that are quadratic in the disturbance velocities are regarded as negligible. On this basis, and after eliminating the pressure perturbation p', a pair of linear partial differential equations is derived for the disturbance velocities u' and v'.

It is then postulated that a typical mode of the disturbance has the form

$$\psi = \phi(y)\, e^{ia(x-ct)}, \tag{6}$$

in which the wave number a is equal to $2\pi/\lambda$, where λ is the wavelength. c is a complex quantity that may be decomposed as

$$c = c_r + ic_i. \tag{7}$$

The real part c_r is the velocity of propagation of the wave and the imaginary part c_i is the amplification factor. It is evident that the flow is stable, neutrally stable,

or unstable relative to the disturbance, according to whether c_i is less than, equal to, or greater than zero. $\phi(y)$ is the amplitude of the disturbance and is, in general, complex. By differentiating (6), one finds

$$u' = \phi'(y)\, e^{ia(x-ct)}, \quad v' = -ia\phi(y)\, e^{ia(x-ct)}. \tag{8}$$

As a final step in the formulation of the stability problem, the foregoing relations for u' and v' are introduced into the linearized equations of motion, from which there follows

$$(\overline{U}-\bar{c})\,(D^2-\alpha^2)\,\overline{\phi}-(D^2\overline{U})\,\overline{\phi} = -(i/\alpha\, Re)\,(D^2-\alpha^2)^2\,\overline{\phi}. \tag{9}$$

This is a dimensionless form of the famous Orr–Sommerfeld equation in which

$$Y = y/\delta, \quad D = d/dY, \tag{10a}$$

$$\overline{U} = U/U_s, \quad \bar{c} = c/U_s, \quad \alpha = a\delta, \quad Re = U_s\delta/\nu, \quad \overline{\phi} = \phi/(U_s\delta). \tag{10b}$$

The boundary-layer thickness is defined here as the distance from the wall at which $U/U_s \cong 0{\cdot}001$, see (5).

The disturbance velocities u' and v' must vanish both at the surface and in the distant environment; that is, $\overline{\phi}$ and $\overline{\phi}'$ are zero at $Y = 0$ and $Y \to \infty$. In the present analysis, in which a numerical solution is contemplated, it is necessary to know the boundary conditions at the edge of the boundary layer. For the region $Y = y/\delta \geqslant 1$, the flow may be regarded as inviscid such that the disturbance equation reduces to

$$\overline{\phi}''-\alpha^2\overline{\phi} = 0. \tag{11}$$

A solution of the foregoing that approaches zero for $Y \to \infty$ is $\overline{\phi} \sim e^{-\alpha Y}$. Thus, the boundary conditions can be stated as

$$\overline{\phi}(0) = \overline{\phi}'(0) = 0, \quad \overline{\phi} \sim e^{-\alpha Y} \quad \text{for} \quad Y \geqslant 1. \tag{12}$$

The mathematical system consisting of (9) and (12) is readily identified as an eigenvalue problem. For prescribed values of α and Re, the task is to find the corresponding value of $\bar{c}$ for which a solution is possible. There are two general approaches to the aforementioned eigenvalue problem. One is the classical technique of asymptotic expansions, which involves functional analysis. This method is well documented by Lin (1955). The second approach is numerical in nature and, owing to the general availability of digital computers, has received much attention in recent years. The present authors have selected the numerical approach for solving the stability problem for the continuous moving surface.

There are two numerical schemes that have been applied with good effect. One of these is based on a step-by-step forward integration of the governing differential equation, for instance Nachtsheim (1963, 1965). The other employs a finite-difference representation, such that the governing differential equation is replaced by a set of algebraic equations. The latter method has been adopted for the present problem.

The finite-difference scheme for investigating the stability of parallel flows appears first to have been used by Thomas (1953) for the case of plane Poiseuille flow. More recently, it has been applied to boundary-layer flows by Kurtz (1961) and Kurtz & Crandall (1962) and by others.

The essential features of the finite-difference scheme are as follows. The region $0 \leqslant Y \leqslant 1$ is subdivided into N points and an algebraic representation of the Orr–Sommerfeld equation is written for each interior point. For the boundary points, $Y = 0$ and $Y = 1$, special equations are written that take account of the boundary conditions. In formulating the finite-difference form of the Orr–Sommerfeld equation, a central-difference representation is supplemented by a subsequent change of variable. The net result of these operations is to provide an algebraic approximation of the participating derivatives having truncation errors of order only h^4, where h is the step size.

By proceeding as described above, a set of N linear, homogeneous, complex algebraic equations is generated. The condition for the existence of a solution is that the determinant of the coefficient matrix be zero. The resulting secular equation containing both real and imaginary parts is

$$F(\alpha, Re, \bar{c}) = 0. \tag{13}$$

If a solution of (13) is available for a given pair of values (α, Re), then the solution corresponding to a nearby pair can be obtained by applying a root-finder technique† first introduced by Muller (1956). The root that is needed to initiate the root-finder technique is deduced by study of a contour map (lines of constant $|F|$) in the complex $\bar{c}$ plane. The details of how this search is carried out is discussed by Kurtz (1961) and Tsou (1965).

The solution of the eigenvalue problem as described above provides all the information necessary to construct a stability diagram, that is, curves of constant $\bar{c}_i$ in the (α, Re)-plane. Moreover, once the eigenvalues are known, then the eigenfunctions can be found by solving the system of linear algebraic equations. From the eigenfunctions, all details of the disturbance flow field can be deduced.

The foregoing discussion provides only a brief account of the numerical formulation of the stability problem. Full details are given by Tsou (1965) and in the published papers of Thomas (1953) and of Kurtz & Crandall (1962). In carrying out the present numerical solutions, careful consideration was given to the size of the finite-difference subdivisions. For various pairs of (α, Re), the secular equation (13) was successively solved for $N = 40, 50, \ldots, 100$, where N is the number of equally spaced points in the range $0 \leqslant Y \leqslant 1$. By extrapolating to $N = \infty$, it was demonstrated that the results for $N = 100$ constituted a highly accurate solution to the problem. This subdivision was therefore employed in the calculations. The eigenvalues thus determined are tabulated in Tsou (1965).

4. The stability diagram and the critical Reynolds number

The solutions of the eigenvalue problem can be brought together on a stability diagram as shown in the lower part of figure 3. This diagram consists of curves of constant $\bar{c}_i$ in the (α, Re)-plane. In this context, the latter quantities are based on the displacement thickness δ^* as the reference length, that is

$$\alpha^* = a\delta^*, \quad Re^* = U_s \delta^*/\nu. \tag{14}$$

† A computer sub-routine is available as share no. RWRF 21.

The contour line corresponding to $\bar{c}_i = 0$ is called the neutral stability curve inasmuch as it separates the unstable region (inside the curve) from the stable region (outside the curve). Five amplification curves characterized by $\bar{c}_i > 0$ are shown inside the neutral stability curve. It is interesting to note that the innermost of these is a closed curve. It is believed that the other amplification curves would show this same characteristic if extended to higher values of Re^*.

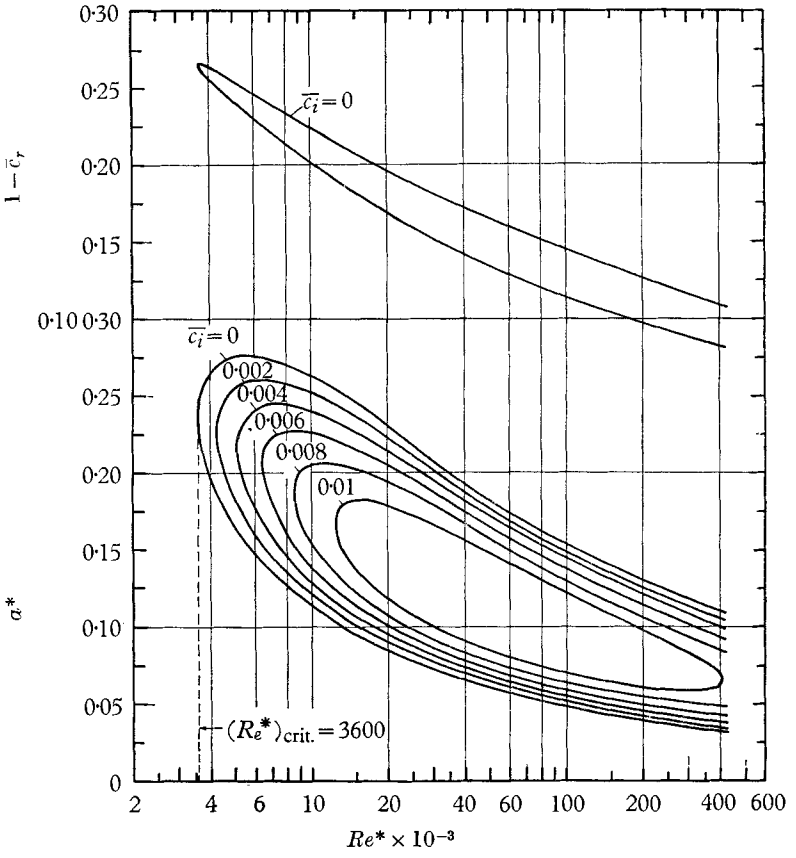

FIGURE 3. Stability diagram.

If a vertical line is constructed tangent to the neutral stability curve, one finds that the corresponding Reynolds number, Re^*, is 3600. Below this value, all infinitesimal disturbances will die out. Thus, for $Re^* < 3600$, the flow is judged to be stable according to small-perturbation stability theory. For any Reynolds number larger than this critical value, the flow will be unstable in some range of α^*. Natural disturbances are regarded as being expandable in a generalized Fourier series, each term of which has the form of (6). Furthermore, natural disturbances are assumed to contain all wave numbers. Therefore, it may be concluded that the flow will become unstable for any Reynolds number larger than the critical.

The mainflow velocity distribution for the continuous-surface boundary layer does not have a point of inflexion. Correspondingly, the flow is stable according

to the theory of inviscid stability. If one associates an inviscid flow with the limit of infinite Reynolds number, it follows that both branches of the neutral stability curve have the abscissa axis as their asymptote as $Re^* \to \infty$. By inspection of the figure, it is seen that the neutral curve shows trends that are consistent with the aforementioned limiting behaviour.

It is of interest to compare the critical Reynolds number for the continuous moving surface just discussed with that for the Blasius flow. This information is summarized in table 1. Re_x is the Reynolds number based on the streamwise co-ordinate x. It is apparent that the critical Reynolds number for the continuous surface is substantially larger than that for the Blasius flow. The former is, therefore, a more stable flow.

	Re^*	Re_x
Continuous surface	3600	$4{\cdot}96 \times 10^6$
Blasius flow (Kurtz & Crandall)	530	$0{\cdot}949 \times 10^5$

TABLE 1. Comparison of critical Reynolds numbers

It is the opinion of the authors that this finding is connected with the fact that the transverse velocity in the mainflow is inward for the continuous surface and outward for the Blasius case. It is believed that the effect of the inflow is to move the disturbances nearer the wall, where they are more readily damped. More information on this point is to be presented in subsequent paragraphs.

An adjunct to the stability diagram is provided in the upper portion of figure 3. This graph shows the values of $(1-\bar{c}_r)$ that correspond to the neutral stability curve. The region of instability is quite narrow in this representation. It is apparent from the figure that $(1-\bar{c}_r)$ decreases with increasing Reynolds number. This implies that the distance from the wall to the critical layer (i.e. the location where $\overline{U} = c_r$ when $c_i = 0$) is smaller as the Reynolds number increases.

It is of particular interest to inquire about the location of the critical layer corresponding to the critical Reynolds number $Re^* = 3600$. From the upper part of figure 3, one finds that, for this condition, $(1-\bar{c}_r) = 0{\cdot}266$. The distance y/δ^* at which $\overline{U} = 0{\cdot}734$ follows from the mainflow velocity profile as 0·37. This is to be contrasted with the fact that y/δ^* corresponding to the critical Reynolds number for the Blasius problem is about 0·75. It is evident that the critical layer for the case of the continuous surface lies much closer to the wall than for the Blasius case. It is believed that this is responsible for the larger critical Reynolds number of the former.

5. The details of the velocity field

The amplitude function

With the eigenvalues now available, the amplitude function can be determined by solving the set of linear algebraic equations that represent the Orr–Sommerfeld equation. To make this algebraic system determinate, it is necessary to specify the value of $\overline{\phi}$ at some point in the boundary layer. For convenience, the condition $\overline{\phi} = 1$ at $Y = 1$ was selected.

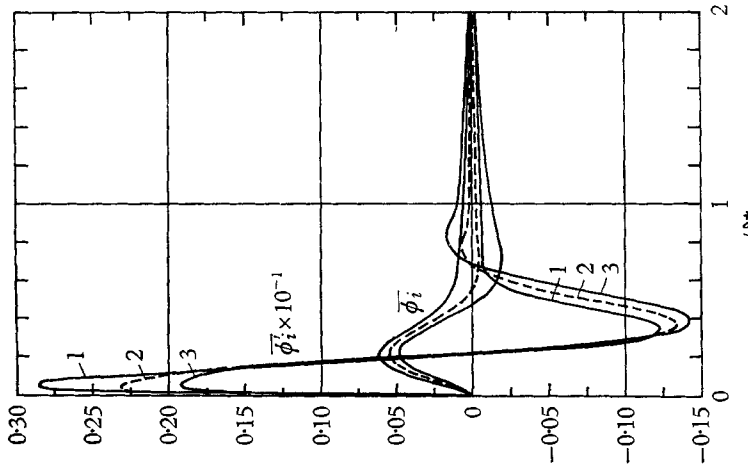

(*b*) The amplitude functions $\overline{\phi}_i$ and $\overline{\phi}_i'$.

	1	2	3
α^*	0·203	0·203	0·203
Re^*	5900	3860	2896
$\bar{c}_r$	0·760	0·741	0·728
$\bar{c}_i$	0·00526	0	−0·00539

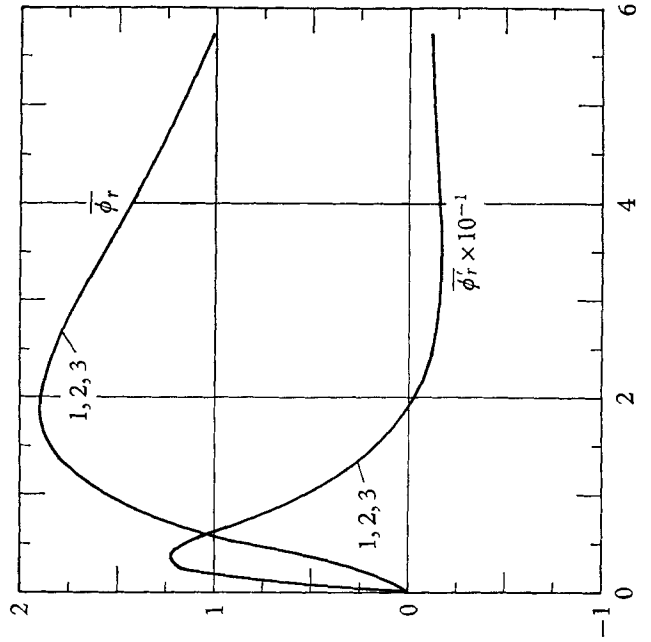

(*a*) The amplitude functions $\overline{\phi}_r$ and $\overline{\phi}_r'$.

	1	2	3
α^*	0·203	0·203	0·203
Re^*	5900	3860	2896
$\bar{c}_r$	0·760	0·741	0·728
$\bar{c}_i$	0·00526	0	−0·00539

FIGURE 4

It was thought that a comparison of the amplitude functions for three points, one in the stable region, one on the neutral curve, and one in the unstable region, would be of interest. To this end, figures 4 (*a*) and (*b*) have been prepared. The conditions characterizing the points are noted in the figures. Figure 4 (*a*) shows the real parts of $\overline{\phi}$ and $\overline{\phi}'$, respectively denoted as $\overline{\phi}_r$ and $\overline{\phi}'_r$. Although the points 1, 2 and 3 are well separated, the corresponding distributions of $\overline{\phi}_r$ and $\overline{\phi}'_r$ are essentially coincident, within the scale of the figure.

The distributions of the functions $\overline{\phi}_i$ and $\overline{\phi}'_i$, which represent the imaginary parts of $\overline{\phi}$ and $\overline{\phi}'$, are plotted in figure 4 (*b*). This figure has a character altogether different from the foregoing. In the present figure, not only do the various curves not coincide, but also they possess different characteristics depending upon the point in question. Further, upon taking cognizance of the different abscissa scales in figures 4 (*a*) and (*b*), it is clear that $\overline{\phi}_i$ and $\overline{\phi}'_i$ decay much faster with increasing distance from the wall than do $\overline{\phi}_r$ and $\overline{\phi}'_r$.

The disturbance velocities and the resultant flow

The components u' and v' of the disturbance flow field are given by (8). Since a velocity is a real quantity, only the real parts of these expressions are taken. The forthcoming discussion will be focused on the neutral stability case; consequently $c_i = 0$. For these conditions, (8) becomes

$$u'/U_s = I[\overline{\phi}'_r \cos a(x - c_r t) - \overline{\phi}'_i \sin a(x - c_r t)], \tag{15a}$$

$$v'/U_s = I[\overline{\phi}_r \sin a(x - c_r t) + \overline{\phi}_i \cos a(x - c_r t)]. \tag{15b}$$

The factor I is a proportionality constant that is introduced in recognition of the fact that the level of $\overline{\phi}$ is arbitrarily assigned (that is, $\overline{\phi}_r = 1$ at $Y = 1$).

By employing (15*a*) and (15*b*), the vector velocity field of the disturbance can be constructed. This has been carried out for the neutral stability case described under point no. 2 in the legends of figures 4 (*a*) and (*b*). The vector field thus obtained is plotted in figure 5. The abscissa of this figure represents a distance of one wavelength in the streamwise direction, while the ordinate gives the distance from the wall. Therefore, the plane of the figure corresponds to the physical space in which the flow takes place. The vector at each point gives the direction and the relative magnitude of the disturbance velocity. The information shown in this figure corresponds to $t = 0$.

From the figure, one sees that the disturbance velocity, which is zero at the wall, increases quite rapidly and reaches a maximum at the critical layer. At still larger distances from the wall, the so-called phase shift occurs; that is, there is a change of sign in the u' velocity component. By studying the column of vectors at either $ax = 0$ or $ax = \pi$, it is seen that the phase shift occurs at $y/\delta^* \cong 1{\cdot}9$. The general appearance of the figure is that of a series of vortices respectively centred at the positions of phase shift on the lines $ax = 0, \pi, 2\pi$, etc. The successive vortices are mirror images of each other as reflected about the planes $ax = -\frac{1}{2}\pi, \frac{1}{2}\pi, \frac{3}{2}\pi$, etc. A diagram having a form similar to that of figure 5 is presented by Kurtz & Crandall (1962) for the Blasius flow.

It is next of interest to construct the resultant flow (mainflow plus disturbance). However, before this superposition can be carried out, it is necessary to specify

the magnitude of the scale factor I that appears in equations (15). In this connexion, use is made of the procedure proposed by Schlichting (1950) for the Blasius flow; that is, the root-mean-square value of u' is averaged across the boundary layer and set equal to 5 per cent of U_s. This choice is made here only for convenience, and nothing is being implied about the limitations on the size of the perturbations that are consistent with linearized theory.

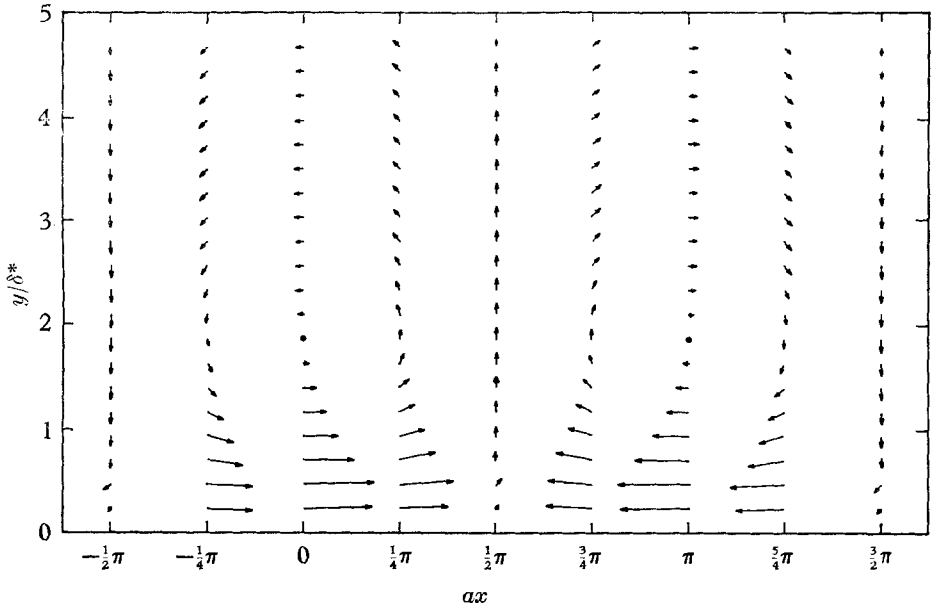

FIGURE 5. The vector velocity field of the disturbance.

Once the scale factor has been determined, the resultant streamwise velocity $(\overline{U}+\overline{u}')$ can be constructed. The computations have been carried out for the same neutral stability case as in the foregoing (point no. 2 in the legends of figure 4) and for $t = 0$. The velocity profiles thus obtained are plotted in figure 6 at four stations, $ax = 0$, $\frac{1}{2}\pi$, π, and $\frac{3}{2}\pi$. The solid lines represent the resultant velocity field, while the dashed lines represent the mainflow.

The resultant velocity profiles at $ax = 0$ and $ax = \pi$ are markedly affected by the disturbance, while those at $ax = \frac{1}{2}\pi$ and $\frac{3}{2}\pi$ are almost coincident with the mainflow. The degree of distortion at other stations will lie intermediate to the aforementioned extremes. In any of the profiles, the largest effect of the disturbance velocity is manifested at the critical layer. At the station $ax = 0$, there is a reverse flow in the outer regions of the profile. These findings are consistent with the vector diagram of figure 5.

Other interesting characteristics of the disturbance flow field include the root-mean-square (r.m.s) velocities. Upon averaging (15) over one period, one finds

$$\sqrt{\widetilde{u'^2}}/U_s = (I/\sqrt{2})\sqrt{(\overline{\phi}_r'^2+\overline{\phi}_i'^2)}, \tag{16a}$$

$$\sqrt{\widetilde{v'^2}}/U_s = (I\alpha/\sqrt{2})\sqrt{(\overline{\phi}_r^2+\overline{\phi}_i^2)}, \tag{16b}$$

where the notation $\sim$ denotes the time average. These expressions are strictly applicable on the neutral stability curve. The scale factor I is determined as described earlier.

The root-mean-square velocity distributions have been evaluated for the same neutrally stable case as previously considered. These results are shown in figure 7, where the u' distribution is the solid curve and the v' distribution is the dashed curve. The former is referred to the left-hand ordinate and the latter to the right-hand ordinate.

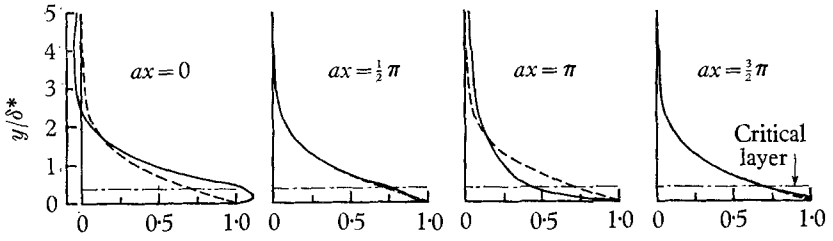

FIGURE 6. The resultant velocity profile (mainflow plus disturbance). ——, Resultant flow, $(U+u')/U_s$; – – – –, mainflow, U/U_s.

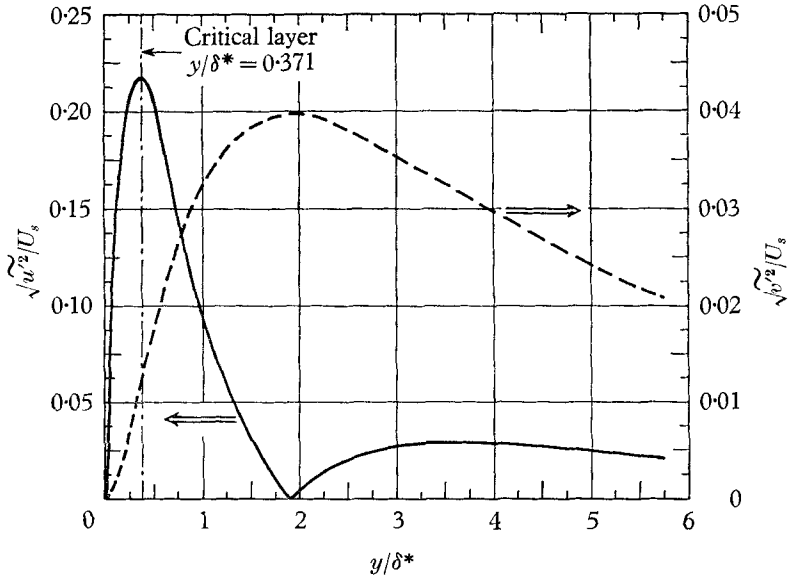

FIGURE 7. Distribution of the root-mean-square disturbance velocities. $\bar{c}_i = 0$; $\alpha^* = 0{\cdot}203$; $Re^* = 3860$.

The distribution of $\sqrt{\widetilde{u'^2}}$ peaks quite sharply at the critical layer, whereafter it decreases and then passes through zero at the point of phase shift. The discontinuous slope at the latter point results from the fact that negative values of u' are suppressed in the presentation of $\sqrt{\widetilde{u'^2}}$. If it had been chosen to plot negative values of $\sqrt{\widetilde{u'^2}}$, then a smooth curve would have resulted. The $\sqrt{\widetilde{v'^2}}$ distribution displays a broader maximum which occurs beyond the critical layer. It is interesting to observe that $\sqrt{\widetilde{v'^2}}$ is much smaller than $\sqrt{\widetilde{u'^2}}$ in the inner portion of the

boundary layer. On the other hand, the two components are of comparable magnitude in the outer portion of the boundary layer.

Two other important characteristics of the disturbance flow are the distributions of the kinetic energy and the Reynolds stress. After suitable manipulation of (15) and (16), one can derive

$$(\widetilde{u'^2}+\widetilde{v'^2})/U_s^2 = \tfrac{1}{2}I^2[\overline{\phi}_r'^2+\overline{\phi}_i'^2+\alpha^2(\overline{\phi}_r^2+\overline{\phi}_i^2)], \tag{17a}$$

$$\widetilde{u'v'}/U_s^2 = \tfrac{1}{2}I^2\alpha[\overline{\phi}_r'\overline{\phi}_i-\overline{\phi}_i'\overline{\phi}_r]. \tag{17b}$$

The numerical evaluation of (17) leads to the distributions that are pictured in figure 8. These results pertain to the same neutrally stable case singled out for prior study.

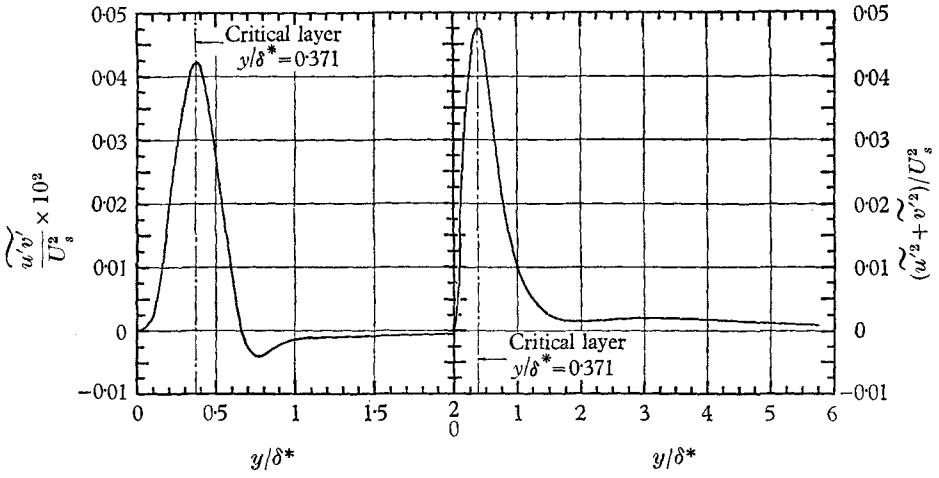

FIGURE 8. Distribution of the kinetic energy of the disturbance and the Reynolds stress. $\bar{c}_i = 0$; $\alpha^* = 0{\cdot}203$; $Re^* = 3860$.

Both the kinetic energy and the Reynolds stress distributions are seen to peak sharply at the critical layer. Beyond their respective maxima, both curves drop off quite rapidly and take on very small values thereafter. It is especially interesting to note that the Reynolds stress is negative over the entire outer portion of the boundary layer.

The aforementioned coincidence of the maxima with the location of the critical layer appears to hold only for points on the neutral stability curve that lie in the neighbourhood of the critical Reynolds number. In the discussion of figure 3, it was noted that the critical layer moves closer to the wall as the Reynolds number increases. The maxima of the u' r.m.s., the kinetic energy, and the shear-stress distributions also move inward, but to a lesser extent. The net result is that these maxima fall beyond the critical layer for larger Reynolds numbers.

6. The energy balance of the disturbance flow

If one considers the momentum equations for the disturbance velocity components, it can be shown (for instance, Schlichting 1950)

$$\frac{dE}{dt} = -\rho \int_{y=0}^{\infty} \int_{x=0}^{\lambda} u'v' \frac{dU}{dy}\, dx\, dy - \mu \int_{y=0}^{\infty} \int_{x=0}^{\lambda} \left(\frac{\partial v'}{\partial x} - \frac{\partial u'}{\partial y}\right)^2 dx\, dy, \tag{18}$$

in which E is the kinetic energy of the disturbance motion contained within a fluid volume extending over one wavelength in x, from the wall to infinity in y, and having unit width, that is

$$E = \frac{\rho}{2} \int_{y=0}^{\infty} \int_{x=0}^{\lambda} (u'^2 + v'^2)\, dx\, dy. \tag{18a}$$

Equation (18) represents the energy balance for the disturbance flow.

The time rate of change of the kinetic energy dE/dt is seen to equal the difference of two quantities that appear on the right. In the first term, a positive $u'v'$ is usually intuitively associated with a negative dU/dY, and a negative $u'v'$ is similarly associated with a positive dU/dY. Therefore, when taken together with its multiplicative minus sign, this term should normally be positive. Physically, this positive characteristic means that energy is drawn from the mainflow into the disturbance flow. Thus, the Reynolds stress term is a de-stabilizing factor. On the other hand, when taken together with its sign, the second term on the right is always negative, since the integrand is intrinsically positive. This term represents energy dissipation and hence is a stabilizing factor.

When $dE/dt < 0$, the rate of energy dissipation by the disturbance exceeds the rate at which energy is supplied by the mainflow. The flow is therefore stable. By similar reasoning, it is evident that the flow is unstable when $dE/dt > 0$ and neutrally stable when $dE/dt = 0$.

It is of interest to investigate the energy balance criterion in the neighbourhood of the neutral stability curve. To this end, (15a) and (15b) are introduced into the energy balance, and after considerable manipulation the following equation can be derived:

$$\frac{d\bar{E}}{d\bar{t}} = \int_0^1 e_R\, dY - \int_0^1 e_D\, dY = E_R - E_D, \tag{19}$$

in which

$$e_R = -\frac{2\pi I^2}{c_1 \bar{c}_r} (\bar{\phi}_r' \bar{\phi}_i - \bar{\phi}_i' \bar{\phi}_r) \frac{dU}{d\bar{Y}}, \tag{19a}$$

$$e_D = \frac{2\pi I^2}{c_1 \bar{c}_r} \left(\frac{1}{\alpha Re}\right) [(\bar{\phi}_r'' - \alpha^2 \bar{\phi}_r)^2 + (\bar{\phi}_i'' - \alpha^2 \bar{\phi}_i)^2]. \tag{19b}$$

The dimensionless variables $\bar{E}$ and $\bar{t}$ are defined as

$$\bar{E} = E/E_0, \quad \bar{t} = t/\tau. \tag{20}$$

The reference quantity E_0 is the kinetic energy of the mainflow contained within a fluid volume extending over one wavelength in x, from the wall to δ in y, and having unit width, that is

$$E_0 = \frac{\rho}{2} \int_{y=0}^{\delta} \int_{x=0}^{\lambda} U^2(y)\, dx\, dy = \frac{\rho \lambda \delta U_s^2}{2} c_1, \tag{21}$$

and

$$c_1 = \int_0^1 \bar{U}^2\, dY = 0{\cdot}094817. \tag{21a}$$

Furthermore, the second reference quantity τ is the time required for the disturbance wave to propagate a distance of one wavelength λ, that is, $\tau = \lambda/c_r$.

It will first be demonstrated that $d\bar{E}/d\bar{t}$ does, in fact, change sign when the neutral stability curve is crossed. To this end, table 2 has been prepared. The table shows results for four points that lie along a vertical line in the (α, Re)-plane near the critical Reynolds number. Two of the points are in the region of stability, while the other two points are in the region of instability. However, as witnessed by the exceedingly small values of $\bar{c}_i$, all points are very, very near the neutral stability curve. Considering the values of $E_R - E_D$, it is evident that $d\bar{E}/d\bar{t} < 0$ for points characterized by $\bar{c}_i < 0$ and > 0 for points characterized by $\bar{c}_i > 0$. It is thereby demonstrated that the present results are consistent with the energy criterion for stability.

Re^*	α^*	$\bar{c}_i \times 10^4$	$E_R \times 10$	$E_D \times 10$
3860	0·203085	−0·570360	0·122311	0·123209
3860	0·203585	−0·227787	0·122834	0·123311
3860	0·204200	0·184197	0·123467	0·123437
3860	0·204600	0·446957	0·123871	0·123521

TABLE 2. Energy balance criterion crossing the neutral curve

Re^*	α^*	$\bar{c}_r$	$\bar{c}_i \times 10^4$	$E_R \times 10$	$E_D \times 10$
3,860	0·203085	0·741386	−0·570363	1·22311	1·23209
10,000	0·113550	0·798849	+0·309486	0·700040	0·696251
34,627	0·068680	0·851985	+0·191973	0·354115	0·352299

TABLE 3. Energy balance criterion for points on the neutral curve

Further information on the energy balance can be obtained by considering several widely separated points that lie on (or very close to) the neutral stability curve.† These points are described in table 3, in which the corresponding values of E_R and E_D are also listed. It may be observed that, in the extreme case, the difference between E_R and E_D is only 0·5 per cent. To give perspective to this finding, comparison may be made with an evaluation of the energy criterion by Schlichting (1950) for the Blasius flow. At two points on the neutral stability curve that was computed by classical asymptotic methods, Schlichting found differences between E_R and E_D of 11 and 14 per cent respectively.

Further insights may be gleaned by inspection of the distributions of e_R and e_D that are shown in figure 9. The figure is divided into three parts that pertain respectively to the three cases described in table 3. For the condition of neutral stability, the area under an e_R curve should equal the area under the corresponding e_D curve.

In general, these functions take on their largest values in the range of small y/δ^* and are of relatively small magnitude for most of the span of the boundary layer. It is for this reason that the curves have been truncated. The maximum value of the dissipation e_D occurs at the wall, where the Reynolds stress contribu-

† These points were actually employed in constructing the neutral curve.

tion e_R is zero. On the other hand, the maximum value of the Reynolds stress term occurs near the critical layer, where the dissipation is essentially zero. The aforementioned maximum is situated to the right of the critical layer at the higher Reynolds numbers. It is also interesting to note that the e_R distribution takes on negative values for a range of y/δ^* after the maximum is achieved. This characteristic was displayed by $\widetilde{u'v'}/U_s^2$ in figure 8. Since the two functions are closely related, this common behaviour is expected.

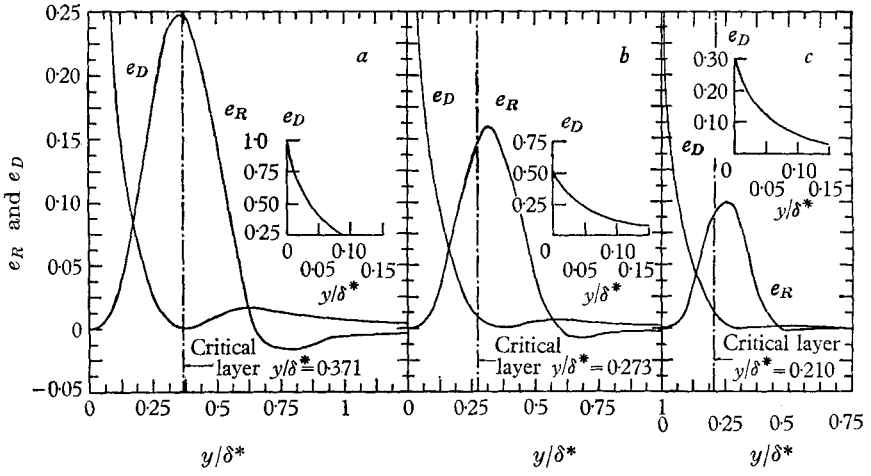

FIGURE 9. Distribution of the dissipation and Reynolds stress terms for the disturbance energy balance. (*a*) $\alpha^* = 0{\cdot}203$; $Re^* = 3860$; $\bar{c}_r = 0{\cdot}741$; $\bar{c}_i = 0$. (*b*) $\alpha^* = 0{\cdot}114$; $Re^* = 10{,}000$; $\bar{c}_r = 0{\cdot}799$, $\bar{c}_i = 0$. (*c*) $\alpha^* = 0{\cdot}069$; $Re^* = 34{,}600$; $\bar{c}_r = 0{\cdot}852$; $\bar{c}_i = 0$.

As the Reynolds number increases, the magnitude and range of the dissipation term are sharply diminished. This is consistent with the approach to the inviscid flow condition. In order to preserve the equality of E_R and E_D, there is a corresponding diminution of e_R.

As a final note, it is interesting to relate the range of y/δ^* encountered in the present results with that predicted by classical asymptotic analysis. In the latter, Lin (1955) postulates that viscous effects are confined to a region adjacent to the wall the thickness of which is proportional to $(\alpha\, Re)^{-\frac{1}{3}}$. Thus, for the three cases considered in table 3 and figure 9, the predicted thicknesses would be 1, 0·89 and 0·69, where all values are taken relative to that for the case $Re = 3860$. Since the viscous layer is not precisely defined, its thickness is taken here as corresponding to the point where e_R is zero. Using this criterion, one may deduce the relative thicknesses from figure 9 as 1, 0·91, and 0·71. The agreement of these values with those mentioned above is quite satisfactory.

The authors wish to express their gratitude to Dr R. J. Goldstein for his suggestions and assistance during the course of this investigation. Thanks are also due to Dr D. D. Joseph for his valuable discussions.

REFERENCES

KOLDENHOF, E. A. 1963 Laminar boundary layer on continuous flat and cylindrical surfaces. *A.I.Ch.E. J.* **9**, 411.

KURTZ, E. F. 1961 A study of the stability of laminar parallel flows. Ph.D. Thesis, Massachusetts Institute of Technology.

KURTZ, E. F. & CRANDALL, S. H. 1962 Computer-aided analysis of hydrodynamic stability. *J. Math. & Phys.* **41**, 264.

LIN, C. C. 1955 *The Theory of Hydrodynamic Stability*. Cambridge University Press.

MIRELS, H. 1961 Laminar boundary layer behind a strong shock moving into air. *NASA TN* D-291.

MULLER, D. 1956 A method for solving algebraic equations using an automatic computer. *Math. Tables Aids Comput.* **10**, 208.

NACHTSHEIM, P. R. 1963 Stability of free-convection boundary-layer flows. *NASA TN* D-2089.

NACHTSHEIM, P. R. 1965 An initial value method for the numerical treatment of the Orr–Sommerfeld equation for the case of plane Poiseuille flow. *NASA TN* D-2414.

SAKIADIS, B. C. 1961*a* Boundary-layer behaviour on continuous solid surfaces: I. Boundary-layer equations for two-dimensional and axisymmetrical flow. *A.I.Ch.E. J.* **7**, 26.

SAKIADIS, B. C. 1961*b* Boundary-layer behaviour on continuous solid surfaces: II. The boundary layer on a continuous flat surface. *A.I.Ch.E. J.* **7**, 221.

SAKIADIS, B. C. 1961*c* Boundary-layer behaviour on continuous solid surfaces: III. The boundary layer on a continuous cylindrical surface. *A.I.Ch.E. J.* **7**, 467.

SCHLICHTING, H. 1950 Amplitude distribution and energy balance of small disturbances in plate flow. *NACA TM* 1265.

SCHLICHTING, H. 1960 *Boundary-layer Theory*. New York: McGraw-Hill.

THOMAS, L. H. 1953 The stability of plane Poiseuille flow. *Phys. Rev.* **91**, 780.

TSOU, F. K. 1965 Velocity field, hydrodynamic stability, and heat transfer for boundary-layer flow along a continuous moving surface. Ph.D. Thesis, University of Minnesota, Minneapolis, Minnesota.